

Sampling the reciprocal Coulomb potential in finite and anisotropic cells

Tobias Schäfer,^{1, a)} William Z. Van Benschoten,² James J. Shepherd,² and Andreas Grüneis¹

¹⁾*Institute for Theoretical Physics, TU Wien, Wiedner Hauptstraße 8-10/136, A-1040 Vienna, Austria*

²⁾*Department of Chemistry, University of Iowa, Iowa City, Iowa 52242, United States*

We present a robust strategy to numerically sample the Coulomb potential in reciprocal space for periodic Born-von Karman cells of general shape. Our approach tackles two common issues of plane-wave based implementations of Coulomb integrals under periodic boundary conditions, the treatment of the singularity at the Brillouin-zone center, as well as quadrature errors, which can cause severe convergence problems in anisotropic cells, necessary for the calculation of low-dimensional systems. We apply our strategy to the Hartree-Fock (HF) and coupled cluster (CC) theory and discuss the consequences of different sampling strategies on the different theories. We show that sampling the Coulomb potential via the widely used probe-charge Ewald method is unsuitable for CC calculations in anisotropic cells. To demonstrate the applicability of our developed approach, we study two representative, low-dimensional use cases: the infinite carbon chain, for which we report the first periodic CCSD(T) potential energy surface, as well as a surface slab of lithium hydride, for which we demonstrate the impact of different sampling strategies for calculating surface energies. We find that our Coulomb sampling strategy serves as a vital solution, addressing the critical need for improved accuracy in plane-wave based CC calculations for low-dimensional systems.

I. INTRODUCTION

Coulomb integrals manifest in numerous theories and models within the domains of many-body physics and quantum chemistry. However, under periodic boundary conditions, numerically modelling the periodic Coulomb potential is a non-trivial endeavour. While its well-known reciprocal form of $4\pi/q^2$ is beyond question, there is no ideal strategy to sample this function in convolutions with electron densities on a discretized grid. Such samplings are necessary for the implementation of computational methods such as the HF theory, Møller-Plesset perturbation theory¹ or CC theories²⁻⁴, to name only a few. While the integrable singularity (at $q = 0$) is the subject of several previous investigations⁵⁻¹², another less studied problem arises when considering anisotropic Born-von Karman (BvK) cells^{13,14}, as in the study of low-dimensional systems. The main target of this work is to enable *ab-initio* many-electron calculations for ground states of low-dimensional systems.

Here, we present an effective sampling technique for the reciprocal Coulomb potential, which is designed for use with anisotropic unit cells. We show how this alleviates the problems that can arise when running many-electron calculations for these systems. The modified potential is universal in character and can just as well be applied to cells of general shape.

II. THEORY

To illustrate the inherent difficulties of the periodic Coulomb potential, we choose the exact exchange energy expression of the Hartree-Fock theory and focus

on the reciprocal space formulation, as it is common in plane-wave based implementations. In the thermodynamic limit (TDL) using atomic units, the exchange energy per unit cell, V , of a periodic system reads¹¹

$$E_x = -\frac{1}{2} \sum_{ij}^{\text{occ.}} \int_{\Omega_{\text{BZ}}} \frac{d^3k}{\Omega_{\text{BZ}}} \int_{\Omega_{\text{BZ}}} \frac{d^3q}{\Omega_{\text{BZ}}} \int_{\mathbb{R}^3} d^3r_1 \int_V d^3r_2 \times \frac{\varphi_{i\mathbf{k}}^*(\mathbf{r}_1) \varphi_{j\mathbf{k}-\mathbf{q}}(\mathbf{r}_1) \varphi_{j\mathbf{k}-\mathbf{q}}^*(\mathbf{r}_2) \varphi_{i\mathbf{k}}(\mathbf{r}_2)}{|\mathbf{r}_1 - \mathbf{r}_2|}. \quad (1)$$

This expression involves a summation over the occupied orbitals φ_i, φ_j , which are normalized in the unit cell, as well as two integrals over the first Brillouin zone with the volume Ω_{BZ} . \mathbf{q} is a momentum transfer vector. The equivalent formulation in reciprocal space allows to replace the two continuous real-space integrals by one discrete sum over all reciprocal lattice vectors, \mathbf{G} ,

$$E_x = -\frac{V}{2} \sum_{ij}^{\text{occ.}} \int_{\Omega_{\text{BZ}}} \frac{d^3k}{\Omega_{\text{BZ}}} \int_{\Omega_{\text{BZ}}} \frac{d^3q}{\Omega_{\text{BZ}}} \sum_{\mathbf{G}} \times \frac{4\pi}{(\mathbf{G} + \mathbf{q})^2} \left| \rho_{ij}^{\mathbf{k}\mathbf{q}}(\mathbf{G}) \right|^2, \quad (2)$$

where we introduced the Fourier transformed co-densities

$$\rho_{ij}^{\mathbf{k}\mathbf{q}}(\mathbf{G}) = \int_V d^3r \varphi_{i\mathbf{k}}^*(\mathbf{r}) \varphi_{j\mathbf{k}-\mathbf{q}}(\mathbf{r}) e^{i(\mathbf{G}+\mathbf{q})\mathbf{r}}. \quad (3)$$

In order to evaluate the exchange energy expression numerically, it is necessary to discretize the two Brillouin zone integrals. In this context, two prominent challenges manifest themselves. First, a discretization inevitably introduces a quadrature error, and second, the presence of the notorious, albeit integrable singularity at $\mathbf{G} + \mathbf{q} = 0$ necessitates careful handling, if the co-densities contain a monopole. In the exchange energy expression this always happens for $i = j$, as $\rho_{ii}^{\mathbf{k},\mathbf{q}=0}(\mathbf{G} = 0) = 1$. We

^{a)}Electronic mail: tobias.schaefer@tuwien.ac.at

note, that these issues originate solely from the used cell shape and discretization grids, which means that no specific class of material is affected, rather all calculations in which Coulomb integrals are used are affected. While an extensive body of literature addresses the singularity issue^{5–12}, less attention has been devoted to mitigating the quadrature error^{13,14}, especially in cases involving anisotropic cell shapes.

For each i, j, \mathbf{k} and \mathbf{G} one has to discretize the integral over \mathbf{q} in the expression of the exchange energy in Eq. (2). This can be re-cast as,

$$I := \frac{1}{\Omega_{\text{BZ}}} \int_{\Omega_{\text{BZ}}} d^3q v(\mathbf{q}) f(\mathbf{q}), \quad (4)$$

which can be considered as the average value of the product of the two functions, $v(\mathbf{q}) := 4\pi/(\mathbf{G} + \mathbf{q})^2$ and $f(\mathbf{q}) := |\rho_{ij}^{\mathbf{k}\mathbf{q}}(\mathbf{G})|^2$. A mesh of N q-points, $\{\mathbf{q}_n\}$, is commonly introduced, in order to discretize Eq. (4) as,

$$I \approx \frac{1}{N} \sum_{n=1}^N v(\mathbf{q}_n) f(\mathbf{q}_n). \quad (5)$$

Typically, so called Monkhorst-Pack meshes¹⁵ or uniform $\mathbf{\Gamma}$ -centered meshes are considered, where $\mathbf{\Gamma}$ is the center of the Brillouin zone (BZ). However, it should be noted that $v(\mathbf{q})$ can vary significantly stronger between the q-points than the co-densities in $f(\mathbf{q})$, in particular if $|\mathbf{G}|$ is small or if the mesh is not equally dense in all spatial dimensions (e.g. in anisotropic cells). This is only the case for the integral over the so called momentum transfer \mathbf{q} , not for the \mathbf{k} integral. The following *exact* reformulation of Eq. (4), where we simply split the integration range into N distinct sub-spaces $\Omega_{\text{BZ}} = \cup_n^N \Omega_{\text{BZ}}^n$, suggests an improved strategy to discretize the \mathbf{q} integral:

$$I = \frac{1}{\Omega_{\text{BZ}}} \sum_{n=1}^N \int_{\Omega_{\text{BZ}}^n} d^3q v(\mathbf{q}) f(\mathbf{q}). \quad (6)$$

If we define the sub-spaces Ω_{BZ}^n as the volume around the points \mathbf{q}_n of the previously introduced q-mesh, and assume $f(\mathbf{q})$ to be roughly constant within the subspace Ω_{BZ}^n , hence $f(\mathbf{q}) \approx f(\mathbf{q}_n)$, we can approximate

$$\begin{aligned} I &\approx \frac{1}{\Omega_{\text{BZ}}} \sum_{n=1}^N f(\mathbf{q}_n) \int_{\Omega_{\text{BZ}}^n} d^3q v(\mathbf{q}) \\ &= \frac{1}{N} \sum_{n=1}^N f(\mathbf{q}_n) \bar{v}_n \end{aligned} \quad (7)$$

where we introduced \bar{v}_n , which only depend on n and \mathbf{G} , as a *mean* Coulomb potential of the subspace Ω_{BZ}^n ,

$$\bar{v}_n(\mathbf{G}) = \frac{1}{\Omega_{\text{BZ}}^n} \int_{\Omega_{\text{BZ}}^n} d^3q \frac{4\pi}{(\mathbf{G} + \mathbf{q})^2}. \quad (8)$$

This formulation, which we abbreviate as "*mean*" in this manuscript, decouples the integration meshes for $f(\mathbf{q})$

and $v(\mathbf{q})$. While conventional q-meshes can be used to evaluate Eq. (7), more sophisticated numerical integration techniques have to be applied to evaluate the deceptively simple integral in Eq. (8). In Sec. IIIB we describe our refined numerical integration technique. Since $\bar{v}_n(\mathbf{G})$ depends only on n and \mathbf{G} , it can be pre-calculated and stored in memory once the lattice and the q-mesh is defined. Using the *mean* strategy from Eq. (7), the final expression for the exchange energy for a mesh of N k-points and q-points finally reads,

$$E_x = -\frac{V}{2} \frac{1}{N^2} \sum_{ij}^{\text{occ.}} \sum_{n,m=1}^N \sum_{\mathbf{G}} \bar{v}_n(\mathbf{G}) \left| \rho_{ij}^{\mathbf{k}_m \mathbf{q}_n}(\mathbf{G}) \right|^2. \quad (9)$$

It is worth noting that this approach addresses both issues: the singularity, and the quadrature errors, which are dominated by the strongly varying Coulomb potential.

The *mean* strategy can readily be applied to Coulomb integrals of any post-HF method. Here, we apply it to the Coulomb integrals for the equations of coupled cluster with single, double and perturbative triple particle-hole excitation operators (CCSD(T)). For more details on the implemented equations in CCSD(T) theory we refer to Ref. 16.

We compare our *mean* strategy with two other common strategies, which are summarized in Tab. I. With "*probe*" we abbreviate the so called probe-charge Ewald method⁷. In the *probe* strategy a usual discretization is performed, as formulated in Eq. (5), but for the singularity at $\mathbf{G} + \mathbf{q} = 0$ the difference between an analytically calculated self-energy of a *probe*-charge and the corresponding numerically computed self-energy using the given q-grid is employed,

$$\begin{aligned} v_0 &= \frac{1}{\Omega_{\text{BZ}}} \int_{\mathbb{R}^3} d^3q \frac{4\pi}{q^2} \varrho(\mathbf{q}) \\ &\quad - \frac{1}{N} \sum_{n=1}^N \sum_{\mathbf{G} \neq 0} \frac{4\pi}{(\mathbf{G} + \mathbf{q}_n)^2} \varrho(\mathbf{G} + \mathbf{q}_n), \end{aligned} \quad (10)$$

with the probe-charge density $\varrho(\mathbf{q}) = 2\sqrt{\alpha/\pi} \exp(-\alpha q^2)$. Commonly, a strongly localized probe-charge is considered, i.e. $\alpha > 0$ but very small, such that v_0 is almost independent of α . The *probe* strategy is the default setting in the VASP code and provides numerically comparable results as the auxiliary function strategy by Gygi and Baldereschi^{5,10}.

Secondly, with "*disr*" we refer to the strategy to simply neglect ("disregard") the grid point at the singularity at $\mathbf{G} + \mathbf{q} = 0$ in the discretization (5). The *disr* strategy is the easiest way to achieve a functional periodic implementation of the Coulomb integral, and is used in some works^{12,17}.

We do not consider the spherical truncation scheme⁹, since it is inadequate for anisotropic BvK cells. The Wigner-Seitz truncation strategy¹¹ is also not considered, as no implementation was available for this work.

strategy	Coulomb potential
<i>mean</i>	$\frac{1}{\Omega_{\text{BZ}}^n} \int_{\Omega_{\text{BZ}}^n} d^3q \frac{4\pi}{(\mathbf{G} + \mathbf{q})^2}$
<i>probe</i>	$\begin{cases} \frac{4\pi}{(\mathbf{G} + \mathbf{q}_n)^2} & \mathbf{G} + \mathbf{q}_n \neq 0 \\ v_0 & \mathbf{G} + \mathbf{q}_n = 0 \end{cases}$
<i>disr</i>	$\begin{cases} \frac{4\pi}{(\mathbf{G} + \mathbf{q}_n)^2} & \mathbf{G} + \mathbf{q}_n \neq 0 \\ 0 & \mathbf{G} + \mathbf{q}_n = 0 \end{cases}$

TABLE I. Comparison of the considered Coulomb kernels for a given sampling grid $\{\mathbf{q}_n\}$ of the Brillouine zone. Note that v_0 was defined in Eq. (10) and Ω_{BZ}^n was defined in the text before Eq. (7).

While preparing this manuscript, it was brought to our attention that an analogous approach was used for GW calculations of excited states in Ref. 18. While it would be of interest to make comparison between the method presented here and Ref. 18, currently no technical capability exists to do so because the method developed here focuses on CC ground-state calculations.

III. METHODS AND IMPLEMENTATION

A. Software and methods

We implemented the *mean* Coulomb potential strategy in the Vienna ab initio simulation package (VASP)¹⁹ and present the implementation in section IIIB. We refer to the associated INCAR tag in VASP as LHFMEANPOT = T.

Through the interface between VASP and the CC4S code²⁰, we can directly compare *mean*, *probe*, and *disr* in periodic HF and CC calculations. All calculations were performed using a plane-wave cutoff of 500 eV. The following projector augmented wave (PAW) pseudopotentials with frozen-core potentials (POTCAR files) were employed for the test systems: PAW_PBE_C_GW_new, Li_GW, and H_GW. The unoccupied space for the CC calculations were compressed to 15 / 12 natural orbitals per occupied orbitals for the carbon chain / LiH system. Natural orbitals are obtained on one-particle reduced density matrices obtained from the RPA²¹ or approximate MP2 level²² of theory. For the carbon chain, a highly effective basis-set correction scheme²³ was employed to approach the complete-basis set limit of the CC correlation energies. Using the *mean* potential, we employed BvK cells with a vacuum of 8 Å and 20 / 10 replicas of the two-atomic unit cell to calculate the potential energy surface of the carbon chain at the HF / CCSD correlation level. The used BvK cells for the LiH slab are discussed in the results section.

B. Implementation of the mean potential strategy

A numerically highly accurate integration of the *mean* potential of Eq. (8) is described in the following, addressing the perils of its seemingly simple form. We partition the integral into a term designed for a radial grid and a term designed for a uniform grid by means of the identity, $1 = e^{-\gamma q^2} + (1 - e^{-\gamma q^2})$, so that we can write,

$$\begin{aligned} & \frac{1}{\Omega_{\text{BZ}}^n} \int_{\Omega_{\text{BZ}}^n} d^3q \frac{4\pi}{(\mathbf{G} + \mathbf{q})^2} = \\ & \frac{4\pi}{\Omega_{\text{BZ}}^n} \left[\int_0^{2\pi} d\varphi \int_0^\pi d\theta \int_0^\infty dq \frac{q^2 \sin\theta e^{-\gamma q^2}}{(\mathbf{G} + \mathbf{q})^2} \Theta_n(q, \theta, \varphi) \right. \\ & \quad \left. + \int_{\Omega_{\text{BZ}}^n} d^3q \frac{1 - e^{-\gamma q^2}}{(\mathbf{G} + \mathbf{q})^2} \right] \quad (11) \end{aligned}$$

where $\Theta_n(q, \theta, \varphi)$ is 1 if the point (q, θ, φ) is in the integration volume Ω_{BZ}^n , and 0 otherwise.

The first integral on the right hand side of Eq. (11) is numerically implemented on a radial grid, whereas the second integral is implemented on a uniform grid along the axes of the reciprocal vectors. Note that no singularity occurs in either integrands. While the Jacobian determinant of the spherical coordinates cancel the singularity in the first integrand, the second integrand approaches the finite value $(1 - e^{-\gamma q^2})/q^2 \rightarrow \gamma$ for $q \rightarrow 0$. In our implementation we set $\gamma = 8 \ln(10) \cdot L_{\text{max}}^2 / (2\pi)^2$, where L_{max} is the largest edge length of the BvK cell. This choice ensures that the factor $e^{-\gamma q^2}$ reaches virtually zero inside the neighboring integration regions, Ω_{BZ}^n , of the region containing the origin $\mathbf{G} + \mathbf{q} = 0$. For all other integration regions, the first integral is virtually zero, and its numerical evaluation can be dropped.

The second integral, using the uniform grid, varies little even at the origin, because of the numerator $1 - e^{-\gamma q^2}$ and by the choice of γ . Thus a relatively small number of grid points can be used. For the integration region containing the origin $\mathbf{G} + \mathbf{q} = 0$, the number of grid points in direction i is chosen according to $N_i \equiv 1000 \text{ \AA} / L_i$, where L_i is the corresponding edge length of the BvK cell in units of Ångström. Based on this number, we halve the number of grid points for each neighboring integration domain, Ω_{BZ}^n , that moves away from the origin.

Finally, we note that smearing the step function $\Theta_n(q, \theta, \varphi)$ improves the convergence of the numerical integration on the radial grid significantly. In our implementation, we multiply Fermi-Dirac-like functions, $(\exp(8d/\Delta q) + 1)^{-1}$, in each direction, to smear the sharp step of Θ_n at the boundaries of the integration regions Ω_{BZ}^n . Here d represents the signed distance between an integration boundary in one direction to the grid point (q, θ, φ) and Δq is the grid spacing of the q coordinate. We use the following radial grid in our implementation: $N_q = q_{\text{max}}/\Delta q \equiv 20$ with $q_{\text{max}} = 2\pi/L_{\text{max}}$, and $N_\varphi = \lfloor 2\pi \cdot N_q \rfloor = 126$, as well as $N_\theta = \lfloor \pi \cdot N_q \rfloor = 63$. The symbol $\lfloor \dots \rfloor$ denotes rounding to the next integer.

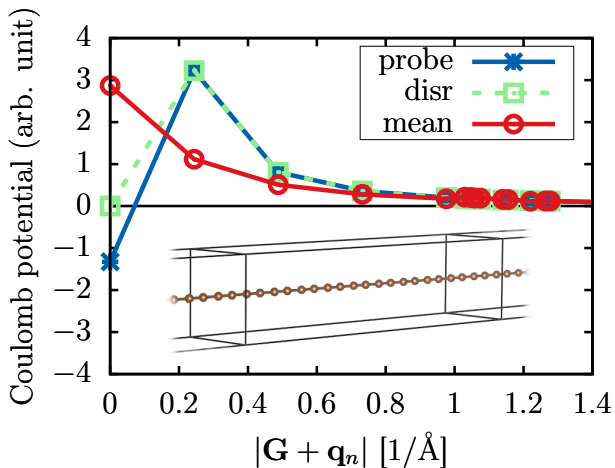


FIG. 1. Comparison of the reciprocal Coulomb potential of the three different sampling strategies, *mean*, *disr*, and *probe* (see text for abbreviations). A BvK cell of the carbon chain with length 25.75 Å (z dimension) and vacuum 6.0 Å (x, y dimension) was used. Due to this geometry, the smallest reciprocal vectors have a magnitude of $|\mathbf{G} + \mathbf{q}_n| = 1.05 \text{ \AA}^{-1}$ in x, y direction and 0.24 \AA^{-1} in z direction.

The described implementation of the *mean* Coulomb potential strategy allows to achieve sub-meV accuracy of the Hartree-Fock energy per unit cell with respect to the number of grid points.

IV. RESULTS AND DISCUSSION

A. Infinite carbon chain

We now turn to our first benchmark system, the infinite chain of carbon atoms in vacuum, where we aim for the calculation of the lattice constant and the bond length alternation, which goes back to a Peierl's distortion²⁴. To our knowledge, no canonical periodic CCSD(T) result was reported in the literature so far. Based on an extrapolation of finite hydrogen-terminated chains, a CCSD(T) result of 0.125 Å was estimated for the infinite chain by Wanko et al.²⁵. However, this is in disagreement with the bond length alternation (BLA) of 0.136 Å and the lattice constant of 2.582 Å from a periodic Diffusion Monte Carlo (DMC) calculation reported in Ref. 26. A further many-electron correlation calculation under periodic boundary conditions was reported by Ramberger and Kresse²⁴ using the random phase approximation (RPA), resulting in a BLA of 0.129 Å, but using a fixed lattice constant of 2.575 Å. Here, we report the first canonical and periodic CCSD(T) result for the BLA and the lattice constant. We calculate five CCSD(T) energies each for BLAs in the range of [0.075 Å, 0.175 Å] and lattice constants in the range of [2.425 Å, 2.725 Å]. These 25 data points are then fitted using the function $E(b, a) = \sum_{n,m=0}^3 c_{nm}(b - b_0)^n(a - a_0)^m$, where b and a

are the BLA and the lattice constant, respectively, and we explicitly neglect the coefficients $c_{11} = c_{31} = c_{32} = c_{13} = c_{23} = c_{33} = 0$. Optimizing the 12 fitting parameters, we find a BLA of $b_0 = 0.128 \text{ \AA}$ and a lattice constant of $a_0 = 2.578 \text{ \AA}$ with a standard deviation of the residuals of 0.5 meV per unit cell. The CCSD(T) data points and a heatmap of the potential energy surface can be found in the supplementary material (SM)²⁷.

These calculations require strongly anisotropic BvK cells, which prohibited previous HF and CCSD(T) calculations, the reasons for which will be evident below. For growing BvK cells in the chain direction, z , the differences of the three strategies *mean*, *probe*, and *disr* are evident for absolute HF energies, as can be observed in Fig. 2(a). While *disr* diverges, both *mean* and *probe* seem to converge to finite, though perhaps slightly different, limits. This is not surprising as with fixed dimensions in x and y , we are not approaching the TDL, which should indeed be unique.

The divergence of *disr* is due to the fact, that we approach the non-integrable singularity of $1/z^2$ at $z = 0$. More precisely, this non-integrable singularity is approached if only the z component of the BvK cell is increased, turning only $\sum_z \rightarrow \int dz$, while $\sum_{x,y}$ remains untouched. Note that in three dimensions, $dx dy dz/(x^2+y^2+z^2) = dr \sin(\theta)d\theta d\varphi$ is free from a singularity, while $dz/(x^2+y^2+z^2)$ possesses a non-integrable singularity for the discrete sampling points $x = y = 0$ at $z = 0$.

The *probe* strategy cancels this divergence of the non-integrable singularity and converges to a finite HF result, as v_0 from Eq. (10) approaches $-\infty$ if only the z dimension of the BvK cell is increased. Both, the value of v_0 and the HF solution of the *disr* strategy approach $-\infty$ for the same reason, as explained above. The negative value of v_0 can be observed in Fig. 1. This *probe* correction provides reasonable results at the HF level of theory, but fails miserably at the CCSD level, as can be seen in Fig. 2(d). Instead of converging to a limit, the CCSD correlation energy falls into the negative and finally the solver fails to converge the CCSD energy after 200 iterations, if the *probe* strategy is used. This is in contrast to *mean* and *disr*, for which the CCSD solver successfully converges for each length of the BvK cell.

We believe that negative values of v_0 are responsible for the deteriorated CCSD energies and for the failure of the CCSD iterations. Note, that the *probe* strategy constructs effectively a pseudized Coulomb potential, as the correction is solely put into the $\mathbf{G} + \mathbf{q} = 0$ component of the potential, here denoted as v_0 . While this pseudization manifests itself only as a shift in the total energy and in the orbital energies at HF theory, it substantially changes the Coulomb integrals in the non-linear CCSD equations. This becomes striking for the Coulomb integrals in the so called ladder contributions. A deeper analysis of the failure of the CCSD iterations is beyond the scope of this work. However, we emphasize that the divergence of v_0 into negative infinity, with increasing z

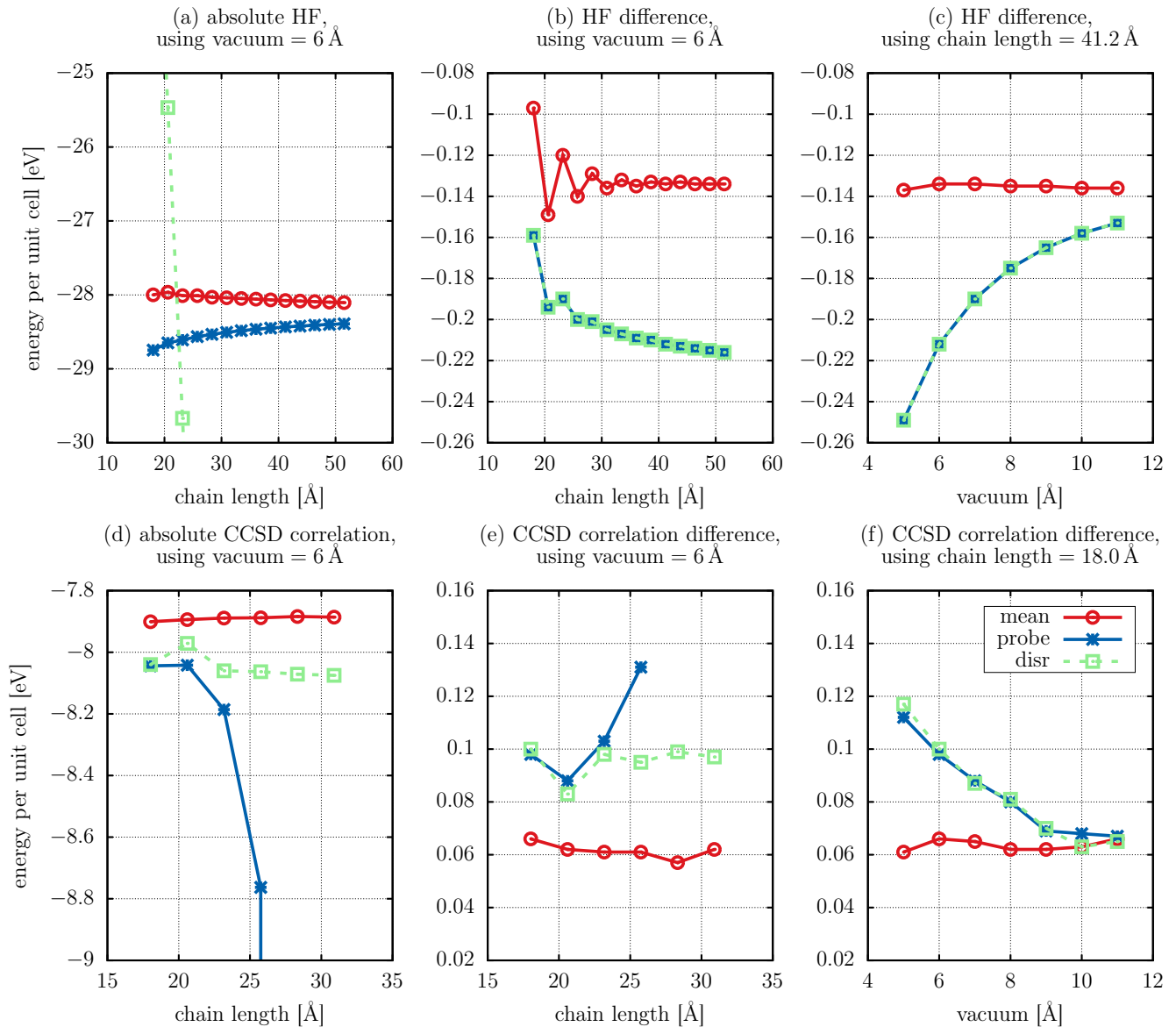


FIG. 2. Convergence of the ground state energy of the carbon chain with respect to length (BvK cell dimension in z direction) and vacuum size (BvK cell dimension in x, y direction) using three different strategies to sample the periodic Coulomb kernel. Absolute energies refer to a BLA of 0.125 \AA , whereas differences refer to the difference between the BLAs 0.075 \AA and 0.125 \AA . The graphs (a)-(c) show the convergence of the HF contribution, whereas (d)-(f) show only the correlation contribution at the CCSD level of theory.

dimension of the BvK cell, entails an underestimation of the mentioned Coulomb integrals. It is conceivable that integrals become negative and thus represent an attractive rather than repulsive electron-electron interaction.

In contrast to the absolute HF energies, the HF energy differences converge only for the *mean* strategy, as is apparent from Fig. 2(b). Here an energy difference between the BLAs 0.075 \AA and 0.125 \AA is considered. Furthermore, it becomes obvious, that both strategies *probe* and *disr* are equivalent for energy difference within the same BvK cell at the HF level. This underlines, that v_0 simply

introduces a constant energy shift in the HF theory.

This is no longer true for the CCSD theory, as evident from Fig. 2(e), which shows the CCSD correlation contribution to this energy difference between the two BLAs. While *mean* provides relatively constant results, with mild but tolerable fluctuations, the failure of the *probe* strategy is markedly visible. Except for one strong outlier, the *disr* strategy here appears to be only shifted to *mean*.

We close the discussion of the convergence behaviour with the dependence on the size of the vacuum, i.e. the

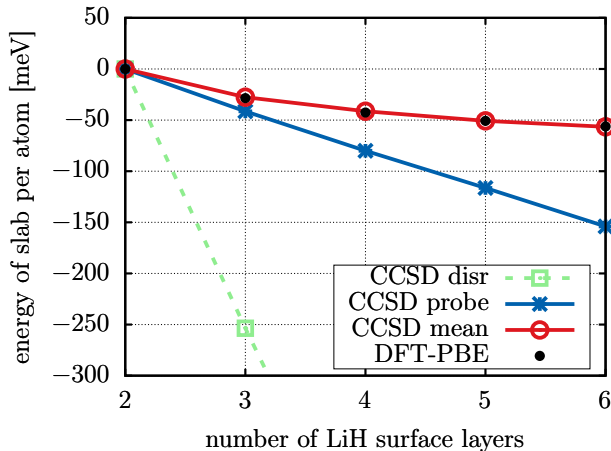


FIG. 3. Convergence of the relative energy of a (001) LiH surface slab per atom with respect to the number of surface layers of the slab. The energies are shifted such that all values agree for the 2-layer slab.

x and y dimension of the BvK cell. In Fig. 2(c), one can see that all strategies seemingly approach the same TDL at the HF level, although at significantly different rates. Note, that the z dimension of the BvK cell is already quite large with 41.2 Å. This is also true at the CCSD level of theory, as depicted in 2(f), since we leave the strong anisotropic regime. Here, a reduced length of 18.0 Å was used.

B. Lithium hydride surface

In our second benchmark system, we address the impact of the different sampling strategies for the electronic ground state of a surface slab model, as necessary for the calculation of surface formation energies or applications in heterogeneous catalysis. The electronic structure of a materials surface determines its physical and chemical properties, i.e. its functionality in scientific and industrial applications. Under periodic boundary conditions, the BvK cells used to model the surface slab can exhibit anisotropic shapes, primarily due to the necessary vacuum above the slab to prevent interactions between periodic images along the normal direction to the surface. Here, we study the impact of the different sampling techniques *mean*, *probe*, and *disr* on the convergence of the per-atom energy of a (001) lithium hydride (LiH) surface slab with respect to the number of surface layers. This energy is a key ingredient for the calculation of surface free energies or for the simulation of surface reconstructions. Note that we do not report a surface energy value for LiH in this study, as this requires calculations outside the primary concern of this work, including the determination of the bulk thermodynamic limit of LiH²⁸ and achieving the basis-set limit.

We model the LiH surface using a $2 \times 2 \times n$ conventional

slab, where we increase the number of layers n from 2 to 6. Each layer consists of 16 atoms, and a vacuum of about 30 Å is added in the normal direction to the slab. The BvK cell of the $n = 6$ layer slab is provided in the SM²⁷.

Figure 3 shows the relative CCSD energy per atom of the LiH surface slabs in dependence of the number of surface layers for different sampling techniques, as well as density function theory results using the Perdew-Burke-Ernzerhofer exchange-correlation functional (DFT-PBE)²⁹. For a better comparison of the convergence behaviour, all energies are shifted to match for the 2-layer slab. For both *probe* and *disr* no convergence of the per-atom CCSD energy can be observed. A differentiated view reveals, that in the case of *probe* the HF energy converges but not the CCSD correlation contribution, and using *disr* it is exactly the opposite. This is documented in the SM²⁷. In contrast, employing the *mean* strategy, the CCSD results converges at nearly the same rate as DFT-PBE. Note that periodic DFT-PBE implementations do not rely on two-electron four-orbital Coulomb integrals and therefore do not suffer from the discussed sampling issues. Thus, the agreement is a strong indication that the *mean* strategy effectively eliminates quadrature errors.

V. SUMMARY AND CONCLUSION

In this manuscript, we have introduced the *mean* Coulomb potential as a sampling technique to enable many-electron ground-state calculations at the level of Hartree-Fock and coupled cluster theory in anisotropic Born-von Karman cells. By examining two illustrative cases, the infinite carbon chain and the (001) LiH surface, we identified and effectively resolved deficiencies inherent in existing sampling techniques for the reciprocal Coulomb potential. The presented implementation for the evaluation of the *mean* Coulomb potential is specifically designed for sub-meV accuracy of ground states and can be directly adopted in other codes employing the reciprocal form of the Coulomb potential. This advancement not only enables predictive *ab initio* calculations for low-dimensional systems using highly-accurate methods like CCSD(T), but can be readily applied to Born-von Karman cells of general shape. Furthermore, the *mean* potential technique can as well be applied without further ado to modified reciprocal Coulomb potentials, such as range-separated potentials^{30,31} or truncated potentials^{9,11,32}, thereby both improving their sampling in reciprocal space and circumventing any special treatment of singularities.

SUPPLEMENTARY MATERIAL

See the supplementary material²⁷ for the CCSD(T) data to calculate the potential energy surface of the car-

bon chain, a decomposition of the CCSD convergence of the (001) LiH surface slab energies into the HF and correlation contribution, as well as the atomic structure of the 6-layer surface slab (POSCAR files).

ACKNOWLEDGEMENTS

T.S. acknowledges support by the Austrian Science Fund through the project ESP 335-N. The computational results presented have been largely achieved using the Vienna Scientific Cluster (VSC). The research presented here was funded in part by the National Science Foundation under NSF CHE-2045046 (J.J.S., W.Z.V).

AUTHOR DECLARATIONS

Conflict of Interest

The authors declare no conflicts of interest.

- ¹C. Møller and M. S. Plesset, “Note on an approximation treatment for many-electron systems,” *Physical Review* **46**, 618–622 (1934).
- ²F. Coester and H. Kümmel, “Short-range correlations in nuclear wave functions,” *Nuclear Physics* **17**, 477–485 (1960).
- ³J. Čížek, “On the correlation problem in atomic and molecular systems. calculation of wavefunction components in ursell-type expansion using quantum-field theoretical methods,” *The Journal of Chemical Physics* **45**, 4256–4266 (1966).
- ⁴I. Shavitt and R. J. Bartlett, *Many – Body Methods in Chemistry and Physics* (Cambridge University Press, 2009).
- ⁵F. Gygi and A. Baldereschi, “Self-consistent hartree-fock and screened-exchange calculations in solids: Application to silicon,” *Physical Review B* **34**, 4405–4408 (1986).
- ⁶G. J. Martyna and M. E. Tuckerman, “A reciprocal space based method for treating long range interactions in ab initio and force-field-based calculations in clusters,” *The Journal of Chemical Physics* **110**, 2810–2821 (1999).
- ⁷J. Paier, R. Hirschl, M. Marsman, and G. Kresse, “The perdew-burke-ernzerhof exchange-correlation functional applied to the g2-1 test set using a plane-wave basis set,” *Journal of Chemical Physics* **122**, 49 (2005).
- ⁸P. Carrier, S. Rohra, and A. Görling, “General treatment of the singularities in hartree-fock and exact-exchange kohn-sham methods for solids,” *Physical Review B - Condensed Matter and Materials Physics* **75**, 205126 (2007).
- ⁹J. Spencer and A. Alavi, “Efficient calculation of the exact exchange energy in periodic systems using a truncated coulomb potential,” *Physical Review B - Condensed Matter and Materials Physics* **77**, 1–4 (2008).
- ¹⁰P. Broqvist, A. Alkauskas, and A. Pasquarello, “Hybrid-functional calculations with plane-wave basis sets: Effect of singularity correction on total energies, energy eigenvalues, and defect energy levels,” *Physical Review B - Condensed Matter and Materials Physics* **80**, 085114 (2009).
- ¹¹R. Sundararaman and T. A. Arias, “Regularization of the coulomb singularity in exact exchange by wigner-seitz truncated interactions: Towards chemical accuracy in nontrivial systems,” *Physical Review B* **87**, 165122 (2013).
- ¹²J. McClain, Q. Sun, G. K. L. Chan, and T. C. Berkelbach, “Gaussian-based coupled-cluster theory for the ground-state and band structure of solids,” *Journal of Chemical Theory and Computation* **13**, 1209–1218 (2017).
- ¹³X. Xing and L. Lin, “Staggered mesh method for correlation energy calculations of solids: Random phase approximation in direct ring coupled cluster doubles and adiabatic connection formalisms,” *Journal of Chemical Theory and Computation* **18**, 763–775 (2022).
- ¹⁴X. Xing, X. Li, and L. Lin, “Unified analysis of finite-size error for periodic hartree-fock and second order møller-plesset perturbation theory,” *Mathematics of Computation* (2023), 10.1090/MCOM/3877.
- ¹⁵H. J. Monkhorst and J. D. Pack, “Special points for brillouin-zone integrations,” *Physical Review B* **13**, 5188 (1976).
- ¹⁶R. J. Bartlett and M. Musiał, “Coupled-cluster theory in quantum chemistry,” *Rev. Mod. Phys.* **79**, 291–352 (2007).
- ¹⁷A. Taheridehkordi, M. Schlipf, Z. Sukurma, M. Humer, A. Grüneis, and G. Kresse, “Phaseless auxiliary field quantum monte carlo with projector-augmented wave method for solids,” *The Journal of chemical physics* **159**, 44109 (2023).
- ¹⁸A. Marini, C. Hogan, M. Grüning, and D. Varsano, “yambo: An ab initio tool for excited state calculations,” *Computer Physics Communications* **180**, 1392–1403 (2009).
- ¹⁹G. Kresse and J. Furthmüller, “Efficiency of ab-initio total energy calculations for metals and semiconductors using a plane-wave basis set,” *Computational Materials Science* **6**, 15–50 (1996).
- ²⁰“Cc4s user documentation,” <https://manuals.cc4s.org/user-manual/index.html>.
- ²¹B. Ramberger, Z. Sukurma, T. Schäfer, and G. Kresse, “Rpa natural orbitals and their application to post-hartree-fock electronic structure methods,” , 1–10 (2019).
- ²²A. Grüneis, G. H. Booth, M. Marsman, J. Spencer, A. Alavi, and G. Kresse, “Natural orbitals for wave function based correlated calculations using a plane wave basis set,” *Journal of Chemical Theory and Computation* **7**, 2780–2785 (2011).
- ²³A. Irmeler, A. Gallo, and A. Grüneis, “Focal-point approach with pair-specific cusp correction for coupled-cluster theory,” *The Journal of Chemical Physics* **154**, 234103 (2021).
- ²⁴B. Ramberger and G. Kresse, “New insights into the 1d carbon chain through the rpa,” *Physical Chemistry Chemical Physics* **23**, 5254–5260 (2021).
- ²⁵M. Wanko, S. Cahangirov, L. Shi, P. Rohringer, Z. J. Lapin, L. Novotny, P. Ayala, T. Pichler, and A. Rubio, “Polyyne electronic and vibrational properties under environmental interactions,” *Physical Review B* **94**, 195422 (2016).
- ²⁶E. Mostaani, B. Monserrat, N. D. Drummond, and C. J. Lambert, “Quasiparticle and excitonic gaps of one-dimensional carbon chains,” *Physical Chemistry Chemical Physics* **18**, 14810–14821 (2016).
- ²⁷See Supplemental Material in the appendix. .
- ²⁸T. N. Mihm, T. Schäfer, S. K. Ramadugu, L. Weiler, A. Grüneis, and J. J. Shepherd, “A shortcut to the thermodynamic limit for quantum many-body calculations of metals,” *Nature Computational Science* **1**, 801–808 (2021).
- ²⁹J. P. Perdew, K. Burke, and M. Ernzerhof, “Generalized gradient approximation made simple,” *Physical Review Letters* **77**, 3865–3868 (1996).
- ³⁰R. D. Adamson, J. P. Dombroski, and P. M. Gill, “Chemistry without coulomb tails,” *Chemical Physics Letters* **254**, 329–336 (1996).
- ³¹J. Paier, M. Marsman, K. Hummer, G. Kresse, I. C. Gerber, and J. G. Ángyan, “Screened hybrid density functionals applied to solids,” *The Journal of Chemical Physics* **124**, 154709 (2006).
- ³²C. A. Rozzi, D. Varsano, A. Marini, E. K. Gross, and A. Rubio, “Exact coulomb cutoff technique for supercell calculations,” *Physical Review B - Condensed Matter and Materials Physics* **73**, 205119 (2006).

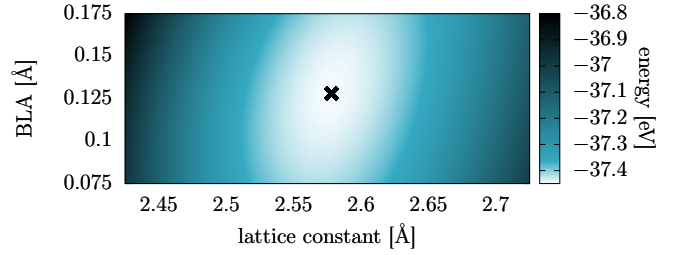


FIG. 4. Heatmap of the potential energy surface of the infinite carbon chain per unit cell in dependence of the BLA and the lattice constant, calculated at the level of CCSD(T). The energy minimum at 2.578 Å, 0.128 Å is denoted by a black x. The necessary information to reconstruct this potential energy surface are provided in the text.

	0.075	0.100	0.125	0.150	0.175
2.425	-36.972	-36.965	-36.934	-36.878	-36.793
2.500	-37.322	-37.331	-37.322	-37.293	-37.242
2.575	-37.413	-37.435	-37.444	-37.437	-37.414
2.650	-37.292	-37.325	-37.347	-37.359	-37.357
2.725	-37.003	-37.043	-37.077	-37.103	-37.119

TABLE II. CCSD(T) ground state energies of the carbon chain per unit cell. A row corresponds to a fixed lattice constant, while a column corresponds to a fixed BLA. The units of energies and lengths are eV and Å, respectively.

Appendix A: CCSD(T) data of the carbon chain

The CCSD(T) results of the carbon chain in dependence of the lattice constant and the BLA can be found in Table II. This data can be used in order to reconstruct the potential energy surface depicted in Fig. 4.

Appendix B: Lithium hydride (001) surface

The total HF and CCSD correlation energy per atom of the LiH surface slabs in dependence of the number of surface layer is shown in Fig. 5. Only for *mean* both the HF and the CCSD correlation contribution converge with respect to the number of surface layers. In the case of the *probe* strategy only the HF energy converges but not the CCSD correlation contribution. In the case of the *disr* strategy the HF energy diverges but the CCSD correlation contribution converges.

The structure of the 6-layer slab of LiH is provided below, in the form of a POSCAR file for VASP:

```
LiH
1.0000000000000000
  8.221600000  0.000000000
0.000000000
  0.000000000  8.221600000
0.000000000
  0.000000000  0.000000000 38.221600000
Li H
```

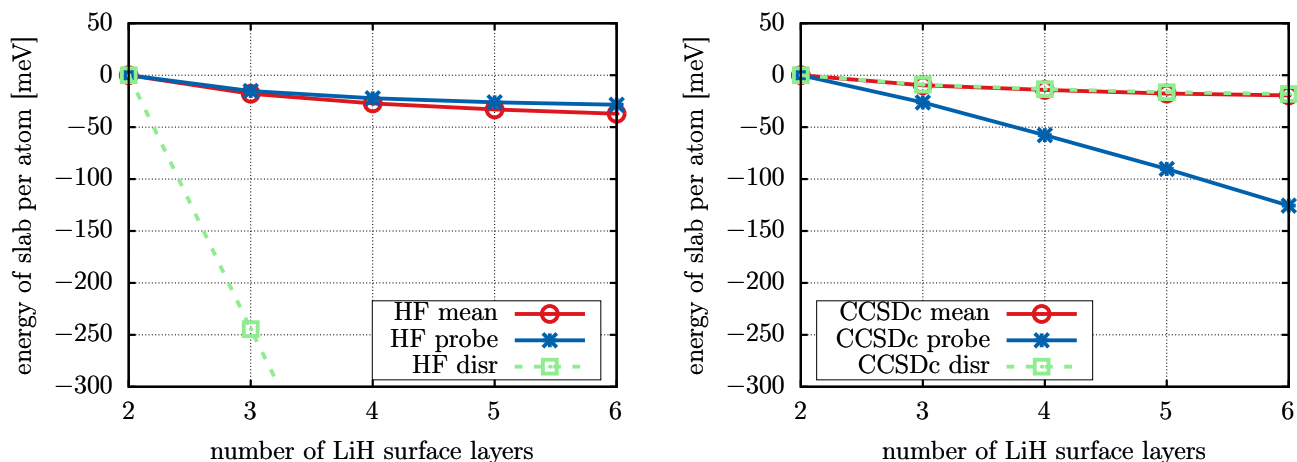



FIG. 5. Convergence of the total energy of a (001) LiH surface slab per atom with respect to the number of surface layers of the slab. In the left plot only the HF contribution is shown, while the right plot shows only the CCSD correlation contribution. The total energies are shifted such that all values agree for the 2-layer slab.

48	48		0.00000000	6.16620000	10.27700000
Cartesian			4.11080000	4.11080000	0.00000000
0.00000000	0.00000000	0.00000000	6.16620000	6.16620000	0.00000000
2.05540000	2.05540000	0.00000000	6.16620000	4.11080000	2.05540000
2.05540000	0.00000000	2.05540000	4.11080000	6.16620000	2.05540000
0.00000000	2.05540000	2.05540000	4.11080000	4.11080000	4.11080000
0.00000000	0.00000000	4.11080000	6.16620000	6.16620000	4.11080000
2.05540000	2.05540000	4.11080000	6.16620000	4.11080000	6.16620000
2.05540000	0.00000000	6.16620000	4.11080000	6.16620000	6.16620000
0.00000000	2.05540000	6.16620000	4.11080000	4.11080000	8.22160000
0.00000000	0.00000000	8.22160000	6.16620000	6.16620000	8.22160000
2.05540000	2.05540000	8.22160000	6.16620000	4.11080000	10.27700000
2.05540000	0.00000000	10.27700000	4.11080000	6.16620000	10.27700000
0.00000000	2.05540000	10.27700000	0.00000000	2.05540000	0.00000000
4.11080000	0.00000000	0.00000000	2.05540000	0.00000000	0.00000000
6.16620000	2.05540000	0.00000000	0.00000000	0.00000000	2.05540000
6.16620000	0.00000000	2.05540000	2.05540000	2.05540000	2.05540000
4.11080000	2.05540000	2.05540000	0.00000000	2.05540000	4.11080000
4.11080000	0.00000000	4.11080000	2.05540000	0.00000000	4.11080000
6.16620000	2.05540000	4.11080000	0.00000000	0.00000000	6.16620000
6.16620000	0.00000000	6.16620000	2.05540000	2.05540000	6.16620000
4.11080000	2.05540000	6.16620000	0.00000000	2.05540000	8.22160000
4.11080000	0.00000000	8.22160000	2.05540000	0.00000000	8.22160000
6.16620000	2.05540000	8.22160000	0.00000000	0.00000000	10.27700000
6.16620000	0.00000000	10.27700000	2.05540000	2.05540000	10.27700000
4.11080000	2.05540000	10.27700000	4.11080000	2.05540000	0.00000000
0.00000000	4.11080000	0.00000000	6.16620000	0.00000000	0.00000000
2.05540000	6.16620000	0.00000000	4.11080000	0.00000000	2.05540000
2.05540000	4.11080000	2.05540000	6.16620000	2.05540000	2.05540000
0.00000000	6.16620000	2.05540000	4.11080000	2.05540000	4.11080000
0.00000000	4.11080000	4.11080000	6.16620000	0.00000000	4.11080000
2.05540000	6.16620000	4.11080000	4.11080000	0.00000000	6.16620000
2.05540000	4.11080000	6.16620000	6.16620000	2.05540000	6.16620000
0.00000000	6.16620000	6.16620000	4.11080000	2.05540000	8.22160000
0.00000000	4.11080000	8.22160000	6.16620000	0.00000000	8.22160000
2.05540000	6.16620000	8.22160000	4.11080000	0.00000000	10.27700000
2.05540000	4.11080000	10.27700000	6.16620000	2.05540000	10.27700000

0.00000000	6.16620000	0.00000000	6.16620000	4.11080000	0.00000000
2.05540000	4.11080000	0.00000000	4.11080000	4.11080000	2.05540000
0.00000000	4.11080000	2.05540000	6.16620000	6.16620000	2.05540000
2.05540000	6.16620000	2.05540000	4.11080000	6.16620000	4.11080000
0.00000000	6.16620000	4.11080000	6.16620000	4.11080000	4.11080000
2.05540000	4.11080000	4.11080000	4.11080000	4.11080000	6.16620000
0.00000000	4.11080000	6.16620000	6.16620000	6.16620000	6.16620000
2.05540000	6.16620000	6.16620000	4.11080000	6.16620000	8.22160000
0.00000000	6.16620000	8.22160000	6.16620000	4.11080000	8.22160000
2.05540000	4.11080000	8.22160000	4.11080000	4.11080000	10.27700000
0.00000000	4.11080000	10.27700000	6.16620000	6.16620000	10.27700000
2.05540000	6.16620000	10.27700000			
4.11080000	6.16620000	0.00000000			